RSC Advances

PAPER

View Article Online
View Journal | View Issue

Cite this: *RSC Adv.*, 2021, **11**, 27701

Effects of the $NiFe_2O_4$ nanoadditive on the performance and emission characteristics of diesel engines: ultrasonic green synthesis by T3 hormone

Samira Mandizadeh,[a] Omid Amiri[bc] and Masoud Salavati-Niasari *[a]

Received 13th June 2021
Accepted 26th July 2021

DOI: 10.1039/d1ra04581d

rsc.li/rsc-advances

$NiFe_2O_4$ nanosheets were successfully synthesized *via* combined ultrasonic and combustion methods using triiodothyronine (T3) hormone as a biotemplate. Isodiesel and heavy diesel were selected as feedstocks to evaluate the ultrasound-assisted catalytic oxidation process. In this study, we focused on high performance of diesel engine with $NiFe_2O_4$ nanosheets. Various conditions such as catalyst dosage, hydrogen peroxide dosage, frequency range and catalyst morphologies of $NiFe_2O_4$ were investigated to achieve optimized conditions. High levels of sulfur compounds (98%) were removed using $NiFe_2O_4$ catalysts under determined conditions (1.0 g L^{-1} catalyst, O/S mole ratio = 2, frequency = 40 kHz and morphology of the nanocatalyst = nanosheets). The nickel ferrite nano additive was mixed with isodiesel and heavy diesel using an ultrasonicator device to achieve better stability. The results indicated that under the optimum amount (1% w/v), the $NiFe_2O_4$ nanostructure is the best additive to reduce NO_x, CO, HC and smoke emission in diesel engines. Moreover, a change in the flash point and viscosity of diesel fuels was observed with the addition of nanosheets. $NiFe_2O_4$ could be recycled 3 times without a significant decrease in catalyst activity.

1. Introduction

Ferrite based nanomaterials with a spinel structure (AFe_2O_4 – A:Ni, Mg, *etc.*) are attractive candidates for a variety of applications such as micro-electronic/magnetic devices and microwave absorbers.[1,2] Nickel ferrite ($NiFe_2O_4$) is one of the best spinel ferromagnetic oxides, where Ni^{2+} and Fe^{3+} ions occupy octahedral and tetrahedral sites, respectively.[3] In general, the purity, physical properties and morphology of $NiFe_2O_4$ govern the performance of the system. For instance, nanocrystalline mesoporous structures with a pure phase are required for catalytic thermo-chemical hydrogen production, and gas sensing applications. To date, different shapes of $NiFe_2O_4$ nanostructures, such as sheets, fibers and rods, have been prepared using co-precipitation, sol–gel, reactive milling, solid state, micro-emulsion, sonochemical, and solvothermal methods. Recently, the ultrasonic method has attracted great attention due to its simplicity, high crystallinity of the product and size control. Among the different shapes of nanoferrite, $NiFe_2O_4$ with two-dimensional (2D) nanosheets provides a large number of accessible active sites, which may lead to good catalytic performance.[4–12]

Recently, utilization of non-toxic, biologically safe, and eco-friendly substances for the synthesis has attracted a lot of attention. The term "biomorphic mineralization" has been recently developed in order to attain nanomaterials with a desired morphology. In recent years, natural materials, like hormones, enzymes, and plant extracts, were applied to prepare nano-sized structures.[13] However, among the natural materials, only few have shown technological interest briefly discussed. In nanomaterials production using biomorphic mineralization, the biotemplates can be used as reducing/capping agents during the reaction. These biotemplates are useful for synthesizing highly ordered morphologies and provide better properties of nanoferrites. Regeneration ability of the ferrites and performing the reactions in short times are important for industrial applications.[14]

Generally, diesel engines are called dirty engines. The control of pollutants in diesel fuel is important due to environmental concerns.[15–18] The incorporation of new technologies in the field of chemistry has improved the efficiency of some chemical reactions. Hydrodesulfurization (HDS) is a new method for sulfur removal; unfortunately, this process requires high pressure and temperature.[19] In recent years, catalytic oxidative desulfurization (CODS) has been developed as a new technology for deep desulfurization of diesel. Different oxidizing agents such as H_2O_2,[20] *t*-butyl-hydroperoxide[21] and ozone[22] have been utilized in this process. H_2O_2 is the mostly selected oxidant due to its environmental compatibility.[23]

Some techniques such as EGR (exhaust gas recirculation),[24] water emulsion,[25] and modifying the engine design[26] have been

[a]*Institute of Nano Science and Nano Technology, University of Kashan, P. O. Box. 87317-51167, Kashan, I. R. Iran. E-mail: salavati@kashanu.ac.ir; Fax: +98 31 55913201; Tel: +98 31 55912383*

[b]*Faculty of Chemistry, Razi University, Kermanshah, 6714414971, Iran*

[c]*Department of Chemistry, College of Science, University of Raparin, Rania, Kurdistan Region, Iraq*

considered to reduce NO_x, HC and smoke emission from diesel engines. Several recent studies have shown that transition metals can be utilized as additives because these crystals help the combustion on the molecular level to achieve better emission reduction.[27,28] Hence, $NiFe_2O_4$ nanosheets were selected as additives in this work. In this study, ultrasound waves were used to assist the ODS process. High local pressure and temperature can be produced by ultrasonic cavitation. They are very reactive and can oxidize sulfur compound to sulfide in fuel. Among the methods for desulfurization, ultrasound-assisted oxidative desulfurization (UAOD) is very important because it does not require expensive equipment and removes sulfur compound under mild conditions. Application of this catalyst in improving diesel quality can pass stringent laws may apply in future.[29–31] Nanomaterials with desired morphologies are the best candidate for improving the catalytic activity. As mentioned before, the production routes/methods generally govern the morphology of the nanomaterials.[32] Moreover, the catalytic performance of the materials also depends on their reaction conditions and the nature in the feed stream.[33]

Apart from various artificial organic templates, we are going to describe natural templates to prepare nanoferrite with improved chemical properties. In the present work, nanosheets of $NiFe_2O_4$ were synthesized *via* an ultrasonic assisted combustion method. To control the morphology of $NiFe_2O_4$, triiodothyronine (T3) hormone was used as a biotemplate. The nanosheet morphology of $NiFe_2O_4$ was used for catalytic oxidative desulfurization. Isodiesel and heavy diesel were selected as the feed to evaluate the catalytic activity. Other parameters such as NO_x, CO, HC and smoke emission were evaluated by adding $NiFe_2O_4$ in the feedstock with an ultrasonicator device.

2. Experimental

2.1 Materials and method

The starting cationic sources $Ni(NO_3)_2 \cdot nH_2O$ (M_w = 290.79 g mol^{-1}, mp = 56 °C, CAS no. 13478-00-7), $Fe(NO_3)_3 \cdot 9H_2O$ (M_w = 404.00 g mol^{-1}, mp = 47 °C, CAS no. 7782-61-8), lactose ($C_{12}H_{22}O_{11}$, M_w = 342.30 g mol^{-1}, CAS no. 63-42-3), and H_2O_2 (30% w/w, CAS no. 7722-84-1) were purchased from Sigma-Aldrich. Triiodothryonine horseradish peroxidase (T3-enzyme conjugate), tetramethylbenzidine (CAS no. 54827-17-7), H_2SO_4 (CAS no. 7664-93-9). All chemicals were supplied in analytical grade and utilized without further purification.

2.2 Synthesis of $NiFe_2O_4$ nanoparticles/nanosheets

T3 hormone was extracted on the basis product sheet provided by Leinco Technologies, Inc.[34] Triiodothyronine (3,5,3′-triiodo-L-thyronine, T3) is produced by the thyroid gland. This hormone controls the body's diverse biochemical processes. T3 was extracted from the thyroid gland and secreted directly into the bloodstream based on the MICRO-EIA T3 test in a solid phase competitive enzyme immunoassay (EIA). In the T3 EIA, a second antibody (goat anti-mouse IgG) was coated on microtiter wells. The test sample was mixed with T3–enzyme conjugate in each well. After 15 min of incubation, the wells were washed to remove any unbounded T3–enzyme. An enzyme chromogen (hydrogen peroxide, H_2O_2, and tetramethylbenzidine, TMB) was added to the well to reflect blue color. To terminate the reaction, 1.0 M H_2SO_4 was added. The sign of reaction quenching can be clearly identified from color tone conversion (blue → yellow). The intensity of the yellow color is important to evaluate the concentration of free T3 in the sample.

Spinel $NiFe_2O_4$ was formulated and synthesized *via* a combustion method. Primarily, the metal nitrates were dissolved in distilled water in stoichiometric ratios. The aqueous solutions were added into the solution containing lactose and stirred for 30 min at 50 °C. Various ratios of lactose : nitrate were selected (0 : 1, 1.5 : 1, 3 : 1 and 6 : 1, samples 1–4) in order to obtain a pure and crystalline product with homogeneous morphologies.

Nanosheets particles were synthesized in the presence of 2 mmol T3 hormone. In a sample containing 6 molar ratio of lactose (sample 4 in this paper), an appropriate amount of T3 hormone (2 mmol) was added, stirred at 50 °C for 30 min and sonicated for 15 min. The obtained product was centrifuged for 10 min at 7000 rpm, decanted, and washed with distilled water and methanol. Finally, all the samples were calcined at 350 °C for 2 hours. A sample containing nitrates, and 6 molar ratio of lactose (sample 5) was synthesized without adding T3 hormone under the same experimental conditions. The preparation conditions are summarized in Table 1. Fig. 1 illustrates a flowchart of an implementation of a general representation of the nanocrystal production method.

2.3 Characterization

X-Ray diffraction (XRD) patterns were obtained from a diffractometer (Philips) with X'PertPro monochromatized Cu-Kα radiation. FESEM (Mira3 Tescan) was utilized to study the morphology of the

Table 1 Preparation conditions, morphology, particle sizes and crystallite sizes of the as-prepared $NiFe_2O_4$ samples

Sample	Lactose : nitrate ratio	Morphology	Average particle size[a] (nm)	Maximum average particle size (nm)	Crystallite size[b] (nm)
Sample 1	0 : 1	Agglomerate	74–175	151–163	3.8
Sample 2	1.5 : 1	Semi-spherical	19–59	20–32	5.0
Sample 3	3 : 1	Agglomerate	71–153	68–75	16.7
Sample 4	6 : 1 + T3	Cuboid/plate	45–80 (height) 234–568 (length) 142–377 (depth)	76–82 284–291 342–350	27.6
Sample 5	6 : 1	Agglomerate	63–159	53–92	15.2

[a] Obtained from Fig. 2. [b] Calculated from the Scherrer equation (Fig. 4).

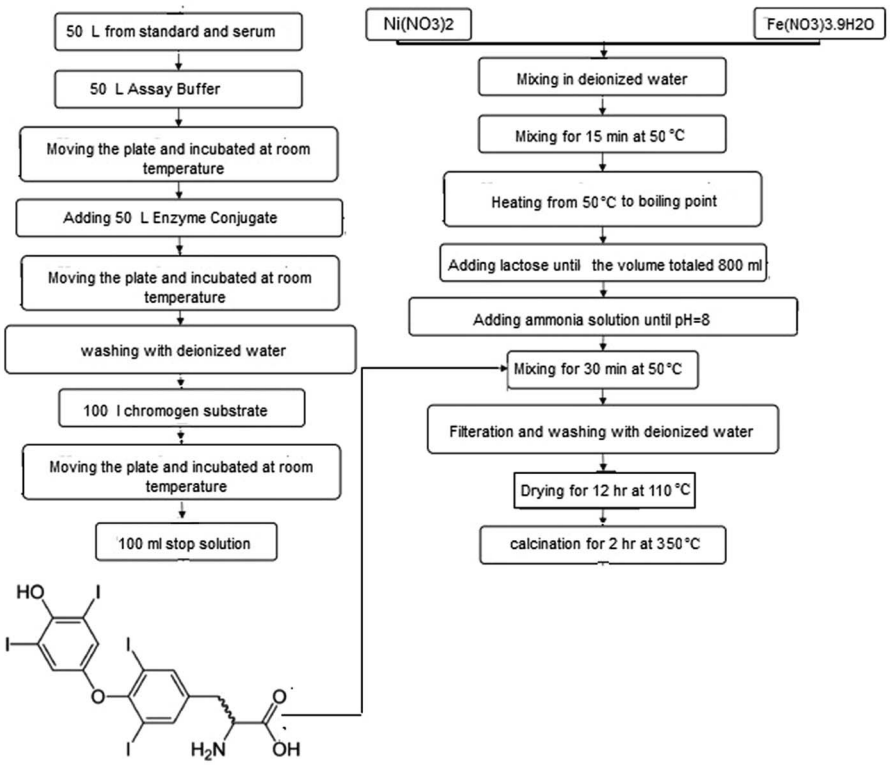

Fig. 1 Preparation of the $NiFe_2O_4$ nanocatalyst.

Table 2 Specifications of the exhaust gas analyzer

Gas	Measuring test	Resolution	Accuracy
CO	0–4000 ppm	1 ppm	±5% of reading or ±10 ppm
HC	0–10% vol	0.01% vol	±0.3% of reading
NO_x	0–4000 ppm	1 ppm	±5% of reading or ±5 ppm
Stack temperature	−20–1315 °C	1 °C	±2 °C
Probe tip temperature	800 °C max	—	—

products. The TEM images and HRTEM images were all obtained using a JEM2100 (JEOL Ltd, Japan). Energy dispersive spectrometry (EDS) analysis was performed using a Philips-XL30 microscope. FT-IR analysis was performed using a Nicolet Magna-IR, 550 spectrometer in KBr pellets. The magnetic properties of the prepared nanocatalysts were studied using a vibrating sample magnetometer (VSM, Meghnatis Kavir Kashan Co., Kashan, Iran). Thermal behavior of the synthesized nanocrystals was examined using a Thermogravimetric Analyzer model Schimadzu TGA-50H (Kyoto, Japan) from 20 °C to 400 °C. The Brunauer–Emmett–Teller (BET) method was used to determine the specific surface area.

2.4 Combustion tests

All combustion tests were performed at a constant engine speed (1500 rpm) and varying engine load ranging from 0 to 12 N m, at equal intervals of 3 N m. Air and fuel consumption rates were measured using an orifice meter (diameter of 20.6 mm) and flow meter sensor (Huba control type 680-out signal 0–10 volts direct current (VDC), accuracy ± 0.25% full scale (FS)), respectively. Cylinder pressure was measured using a Kistler piezoelectric pressure sensor of Model 6052C connected to a charge amplifier (Model GUNT CT100.13), while the engine speed was measured through a proximity sensor (WACHENDORFF of type PNP-N. O, Sn 4 mm, 10-30VDC, and 200 mA). A k-type thermocouple was applied to determine the exhaust gas temperature from the engine diesel after adding the catalyst in an amount of 1%. NO_x, CO, HC and smoke emission were measured using an AVL Di-gas and AVL 437C, respectively. The feedstock was pumped to the engine diesel with a standard injection pressure of 201 bar and injection timing of 24° bTDC.

Table 3 The details of the engine test

Make & Model	Kirloskar TAF1
Type: Four stroke	Single cylinder,
Direct injection	Bore X stroke (mm): 87.5 × 110
Compression ratio	17.5 : 1
Engine capacity	0.661 litre
Rated power	4.4 kW
Rated power rated speed	1500 rpm (constant speed)

Table 4 Uncertainties of experimental measurements

Instrument	Range	Accuracy	Uncertainty
Torque indicator, N m	0–200	±1% of reading	1
Fuel burette, cc	153	±0.2	1
Speed sensor, rpm	0–10000	±5 rpm	0.1
CO, ppm	0–4000	±10 ppm	1
UHC, % vol	0–10% vol	±0.3% of reading	0.1
NO_x, ppm	0–4000	±5 ppm	1
Pressure transducer, bar	250	±1% of reading	1
Crank angle encoder, degree	0–720	±0.5	0.3
Brake power	—	—	±1

Engine emissions were measured with an ECA 450 exhaust gas analyzer. The exhaust gas sample was dried prior to analysis. The technical specifications of the emission analyzer are given in Table 2. An ASTM D445 (Anton Paar, Austria) and ASTM 93 were used to measure viscosity and flash point, respectively. The details of the engine test are tabulated in Table 3.

The experimental uncertainties in the presented results were evaluated according to the root sum square method. Table 4 gives the uncertainties of the various measuring devices used in the present study.

2.5 Desulfurization activity and reusability of the catalyst

The isodiesel and heavy diesel (Markazi Province, Iran) were selected as the feedstocks. Table 5 shows the main characteristics of the feedstocks. The reactions were performed in a fixed-bed microreactor. In a glass reactor, the experiments were directed in batch with a 20 kHz ultrasonic processor. A specific amount of model fuel (100 ml) and hydrogen peroxide 30% were added to the reactor. To maintain temperature, a water bath was employed. After maintaining the selected temperature, the mixture was sonicated for 15 min. After cooling at room temperature, the mixture was centrifuged for 10 min. The main characteristics of the product and feedstock were evaluated *via* the analytical methods: analysis of sulfur compound was performed using an X-ray sulfur analyzer (Korea). For industrial applications, the regeneration unit of the catalyst is important in selecting the catalyst for the ODS process. In the current study, the regeneration ability of the catalyst was investigated at elevated temperature (600 °C) in the presence of N_2 gas. In the end of the reaction, the liquid feed containing the catalyst (1 g L^{-1}) is pumped up to the reactor, and the catalyst was recovered by filtration, washed with acetonitrile and calcined at 600 °C.

Table 5 Results of the viscosity and flash point tests for fuels with and without additives

Properties	Iso diesel	Heavy diesel	Concentration of the nanostructure
Viscosity (40 °C) (mm^2 s^{-1})	5.3	11.2	0 ppm
	6.72	12.33	1% by volume
Flash point (°C)	126	167	0 ppm
	134	175	1% by volume

3. Results and discussion

3.1 Structural analysis

Fig. 2 shows the XRD patterns of the as-made $NiFe_2O_4$ samples. As mentioned in Table 1, in a constant stoichiometric amount of cationic sources, the ratio of fuel was changed. In the sample without lactose, sample 1, the XRD pattern is not highly crystalline and only three peaks grow at 2θ equal to 35.97°, 44.12°, and 63.06° (Fig. 2a). Upon an increase in lactose concentration, the diffractograms contain peaks as compared to sample 1. These patterns match JCPDS 44-1485. However, Fe_2O_3 and NiO appear along with the major phase (Fig. 2b and c). The amounts

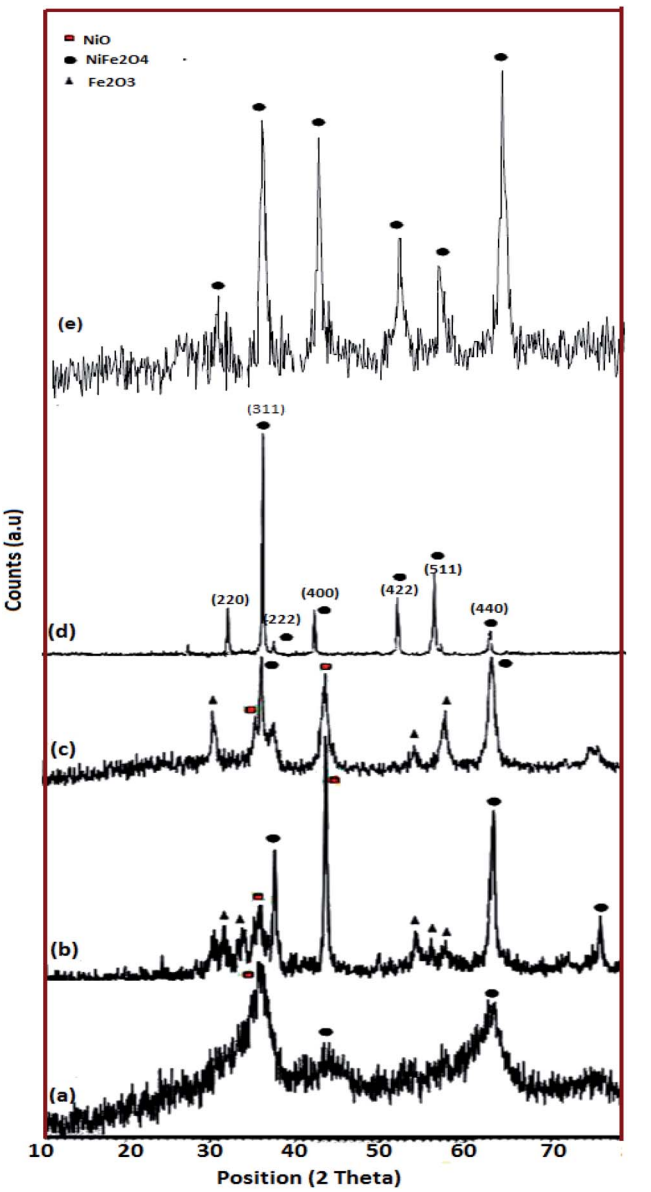

Fig. 2 XRD patterns of the as-prepared $NiFe_2O_4$; (a) sample 1 ($NiFe_2O_4$ prepared without lactose), (b) sample 2 ($NiFe_2O_4$ prepared with 1.5 mol ratio lactose), (c) sample 3 ($NiFe_2O_4$ prepared with 3 mol ratio lactose), (d) sample 4 (hormone treated $NiFe_2O_4$) and (e) sample 5 ($NiFe_2O_4$ prepared with 6 mol ratio lactose).

of impurities are more obvious in sample 2 (Fig. 2b) as compared to sample 3 (Fig. 2c). The major phase in sample 2 grows at 30.45°, 35.85°, and 63.10°. The diffraction peaks of sample 3 and sample 4 are more intense as compared to sample 1. Fig. 2d and e show pure spinel $NiFe_2O_4$ and the diffraction peaks are observed at 30.36°, 35.70°, 43.40°, 57.36°, and 63.01°. The average crystallite size was calculated by Scherrer equation eqn (1),

$$D = k\lambda/\beta \cos\theta, \quad (1)$$

which was obtained to be around 3.8, 5.0, 16.7, 27.6, and 15.2 nm, for the samples 1, 2, 3, 4 and 5, respectively. In the Scherrer equation, D is the size of nanoparticles, λ is the X-ray wavelength, β is the line broadening at half the maximum intensity, k is a constant and θ is the diffraction of the peak.

3.2 Morphology and physico–chemical properties of hormone treated $NiFe_2O_4$ nanosheets

The impact of reductant concentrations on the surface morphology and the particle size of the samples were investigated using FESEM (Fig. 3a–e). It is clear that in the sample without lactose, the majority of the particles are agglomerated (Fig. 3a). Upon increasing lactose ratio to 1.5 (Fig. 3b), semi-spherical particles were formed, in a homogeneous texture. Fig. 3c and d show the $NiFe_2O_4$ samples synthesized with lactose/nitrate molar ratios of 3 : 1 and 6 : 1, respectively. In the latter morphology, the particles agglomerate, while in the former, cuboid (plate) structures are obtained. Each molecule of T3 hormone contains functional groups. These functional groups are iodine, amine and carboxylic acid in which T3 contains three iodide groups. These functional groups may react with metal nitrates and create weak links to form complex ions. Under the ultrasonic conditions, high temperature and pressure induce the complexes to decompose into the $NiFe_2O_4$ nanocrystals. To reduce the Gibbs free energy,[35] primary particles deposit on the larger crystal's surface to form homogeneous regular shapes. T3 hormone has an important role in the formation of the one-dimension growth. The long chain of T3 molecules is absorbed on the various crystal planes, and acts as some face inhibited function surfactant to help competitive growth to form a sheet like morphology. Morphological observation of hormone treated $NiFe_2O_4$ confirms the formation of very thin nanosheets (Fig. 3d). In Fig. 3e (sample without T3 hormone), a large quantity of cubic structure can be observed. The results from morphological observations are tabulated in Table 2. The grain size estimated from FESEM data was discerned to be larger than the one obtained from XRD analysis. This indicated that every grain was formed by the aggregation of several tiny ferrite nanocrystallites or nano-particles.

The FTIR spectrum of the sample 4 (Fig. 4a) shows two intense bands at 588 cm^{-1} and 437 cm^{-1}, which are related to the stretching vibration of Fe–O and Ni–O, respectively. The bands at 3436 cm^{-1} and 1630 cm^{-1} are due to the moisture (H–OH).[36] The EDS analysis clearly affirms the presence of Ni, Fe and O in the hormone treated $NiFe_2O_4$ composition (Fig. 4b).

The $NiFe_2O_4$ hormone treated sample was selected in order to investigate the physico–chemical properties of this sample. Primarily, specific surface area was determined using Brunauer–Emmett–Teller (BET). The N_2 adsorption/desorption isotherm can be observed in Fig. 4c. The obtained average pore diameter and specific pore volume of the $NiFe_2O_4$ nanosheets were 9.53 nm and 7.62 $cm^3\ g^{-1}$, respectively. A porous structure with a BET surface area of 24.2 $m^2\ g^{-1}$ was obtained, which can be classified as isotherm type IV and H3-type hysteresis. The H3-type hysteresis loop confirms mesoporous materials according to the IUPAC classification. The H3-type hysteresis shows the random distribution of pores. As a result, there is a significant increase in the BET surface area compared to other studies.[37]

The T3 treated sample powder was subjected to simultaneous thermogravimetric analysis (TGA) (Fig. 4d). The sample decomposed in three steps, 50–150 °C, 170–300 °C and 340–750 °C. The first weight loss region from 50 °C to 150 °C is related to the dehydration of water in the precursor sample. The weight loss at 170–300 °C could be due to the oxidation of organic materials and the third weight loss region represents the crystallization or phase formation process of $NiFe_2O_4$.

VSM is a standard method to evaluate the magnetic properties of the hormone treated sample. Fig. 4e depicts the magnetic hysteresis loop. The saturation magnetization (M_s), remanence magnetization (M_r) and coercivity (H_c) values for the sample are 1.22 emu g^{-1}, 0.08 emu g^{-1} and 80 Os respectively. Therefore, the $NiFe_2O_4$ nanostructure shows ferromagnetic behavior. The magnetism of the catalyst plays an important role in separation of the catalyst after the desulfurization process.

3D observation of the sample (Fig. 5a–d) clearly shows that the $NiFe_2O_4$ formed with a nanosheet morphology with nanometer dimensions of around 466 nm × 2 nm. The corresponding high-resolution TEM (HRTEM) is shown in Fig. 5d, which shows the single-crystalline nature of these 2D nanosheets, with lattice spacings of 0.48 nm and 0.276 nm, in agreement with the (111) and (311) planes of $NiFe_2O_4$.

3.3 Catalytic activity

Oxidative activities of the synthesized $NiFe_2O_4$ nanostructure in different shapes of $NiFe_2O_4$ (semi-spherical and sheet) were studied with iso and heavy diesel as feedstocks and are shown in Fig. 6.

The significant changes in sulfur removal were observed during oxidative desulfurization by using different catalyst morphologies (Fig. 6a and b). Decomposition of sulfur compound can be influenced by basic or acidic sites present in the structure. The catalytic properties of $NiFe_2O_4$ nanostructures strongly depend on the nickel and iron ions and their distribution between the octahedral and tetrahedral sites that may enhance the extent of interactions of the phases at the border line during the desulfurization process. For instance, Ni and Fe are basic elements that can improve the decomposition of sulfur compound. The result indicates that the nanosheet morphology of $NiFe_2O_4$ has higher activity as compared to the other structures of $NiFe_2O_4$. This is most probably due to the high surface area of nanosheet morphology. Catalytic performances of cube $NiFe_2O_4$ (sample 5) are shown in Fig. 6. The results

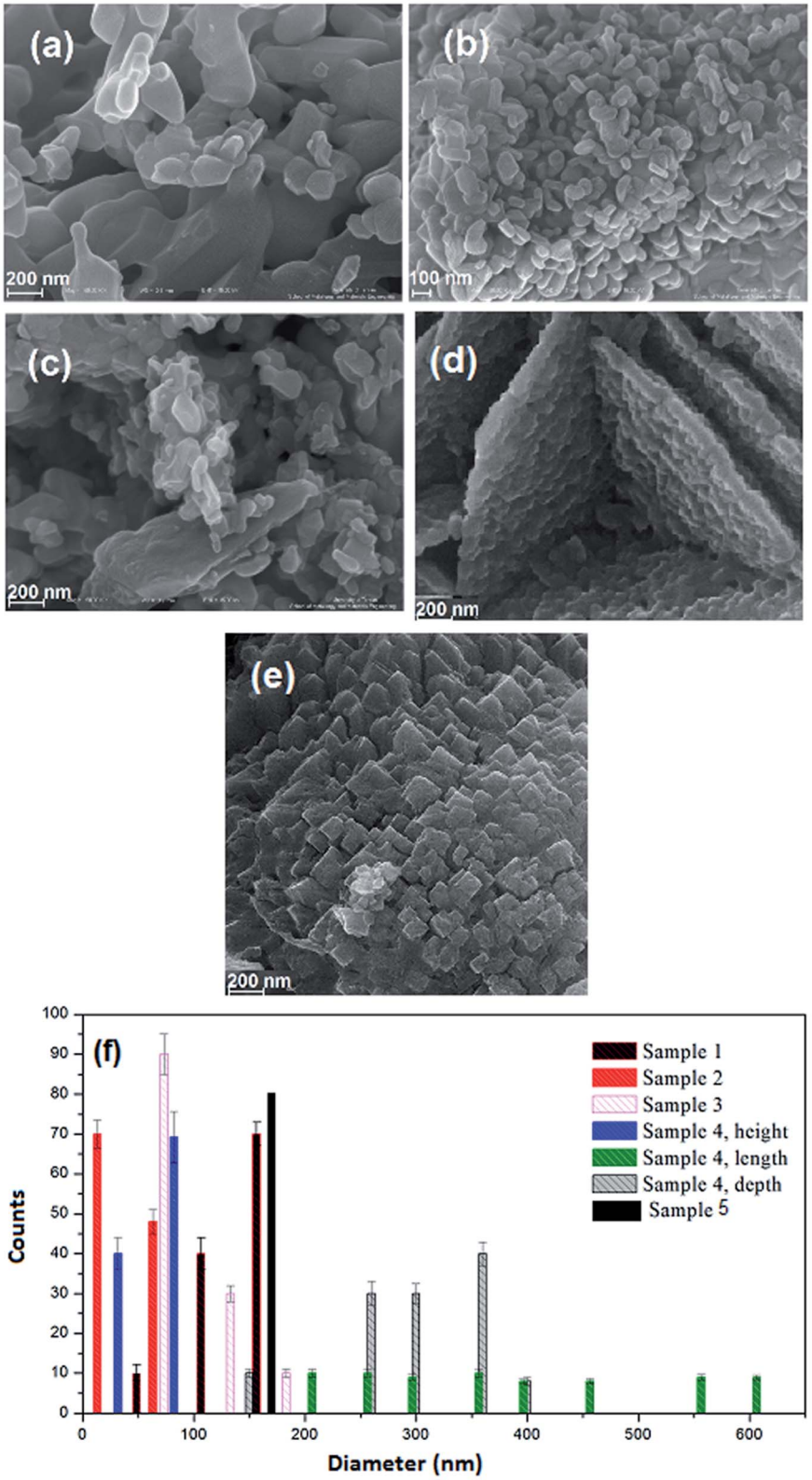

Fig. 3 FESEM micrographs of $NiFe_2O_4$ prepared in various reductant : nitrate ratios; (a) sample 1 ($NiFe_2O_4$ prepared without lactose), (b) sample 2 ($NiFe_2O_4$ prepared with 1.5 mol ratio lactose), (c) sample 3 ($NiFe_2O_4$ prepared with 3 mol ratio lactose), (d) sample 4 (hormone treated $NiFe_2O_4$), (e) sample 5 ($NiFe_2O_4$ prepared with 6 mol ratio lactose) and (f) their respective histograms.

indicate that poor catalytic performance of cube-$NiFe_2O_4$ is due to a lower number of active sites on the surface of the catalyst, resulting in decreasing catalytic activity.[38]

Fig. 6c and d depicts that the sulfur removal from fuel can be increased on the basis of catalyst concentration with the nanosheet morphology from 0.5 to 1.0 g L^{-1}. For isodiesel, the

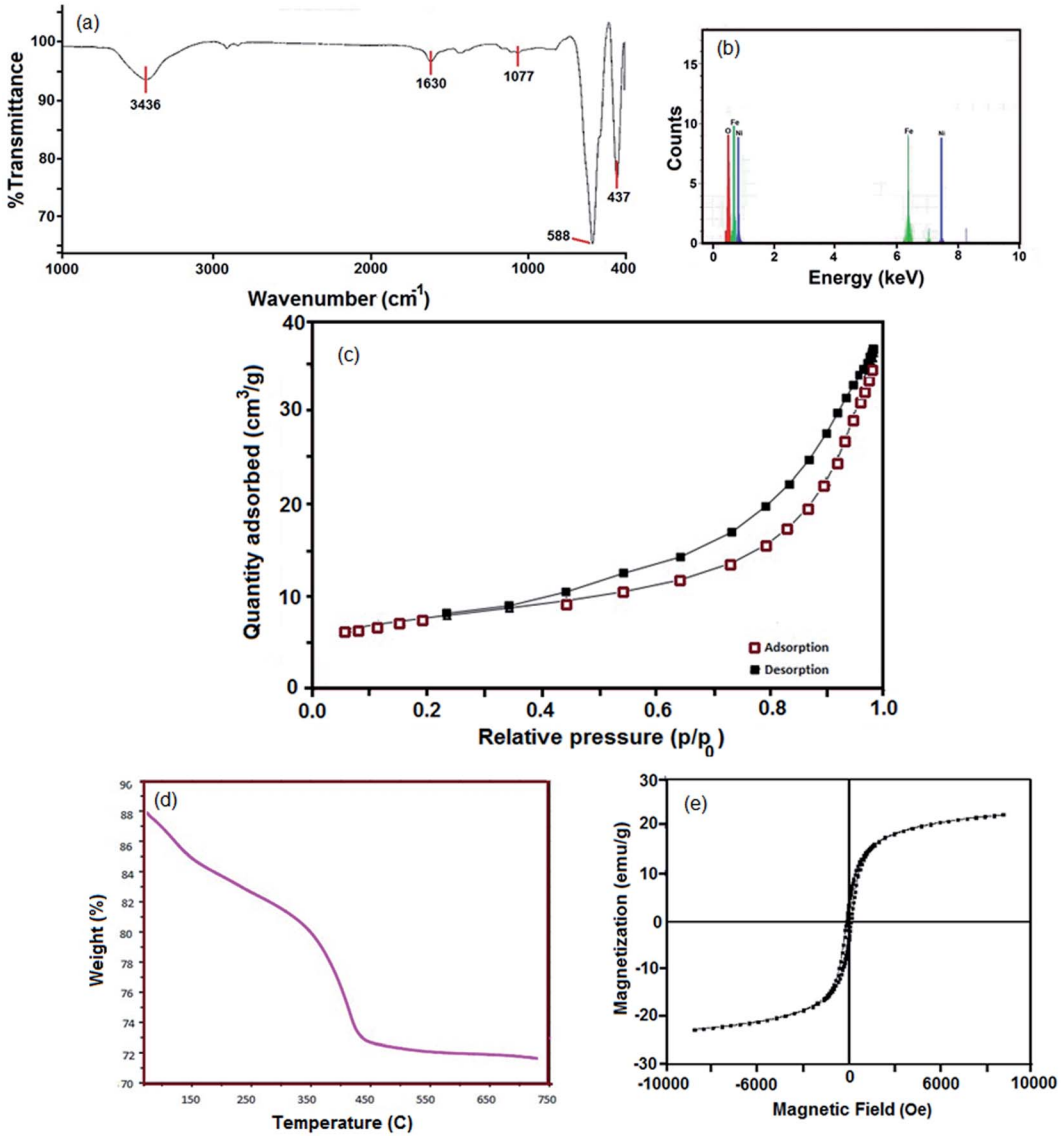

Fig. 4 (a) FTIR spectrum of hormone treated $NiFe_2O_4$ nanosheets (sample 4), (b) EDS spectrum of hormone treated $NiFe_2O_4$ nanosheets (sample 4), (c) N2 adsorption/desorption isotherm, (d) TG analysis and (e) magnetization hysteresis loops of hormone treated $NiFe_2O_4$ nanosheets (sample 4).

removal rates for 0.5 and 1.0 g L^{-1} were estimated to be around 45% and 70% at constant time (45 min), respectively. The number of active sites on the catalyst surface is directly related to the catalyst dose. The results reveal that the $NiFe_2O_4$ can be utilized as a new catalyst for sulfur removal.

Fig. 6e and f shows that the sulfur removal can be influenced by the concentration of H_2O_2. Increasing the concentration of H_2O_2 can be effective in removing sulfur compounds. For the two types of diesel fuels, the best results were obtained when the volume ratio of H_2O_2 to fuel is 1 : 2. Increasing concentration of H_2O_2 provides more oxidizing agents such as OH. Hence, desulfurization rate is greatly increased. During the ultrasonic process, H and OH radicals were generated by water pyrolysis. Different reactions to produce radicals are mentioned below:

$$HO^{\circ} + H_2O_2 \rightarrow HO_2^{\circ} + H_2O$$

$$H_2O_2 + OH^- \; HO_2^- + H_2O$$

Effects of ultrasonic frequency are described in Fig. 6g and h. It showed that useful results are obtained with a frequency of 40 kHz for the two types of diesel fuels. The elimination rate of sulfur compound reached 20.8% and 70.3% with frequencies of 20 and 40 kHz at 70 °C for 20 min of sonication in the system of H_2O_2–$NiFe_2O_4$-isodiesel, respectively. Sulfur removal rates were enhanced by an ultrasound probe in the UAOD process due to its smoother dispersion capability and high local temperatures and pressures.[39]

To improve the quality of diesel fuel, $NiFe_2O_4$ nanosheets were selected and doped in isodiesel and heavy diesel to reduce

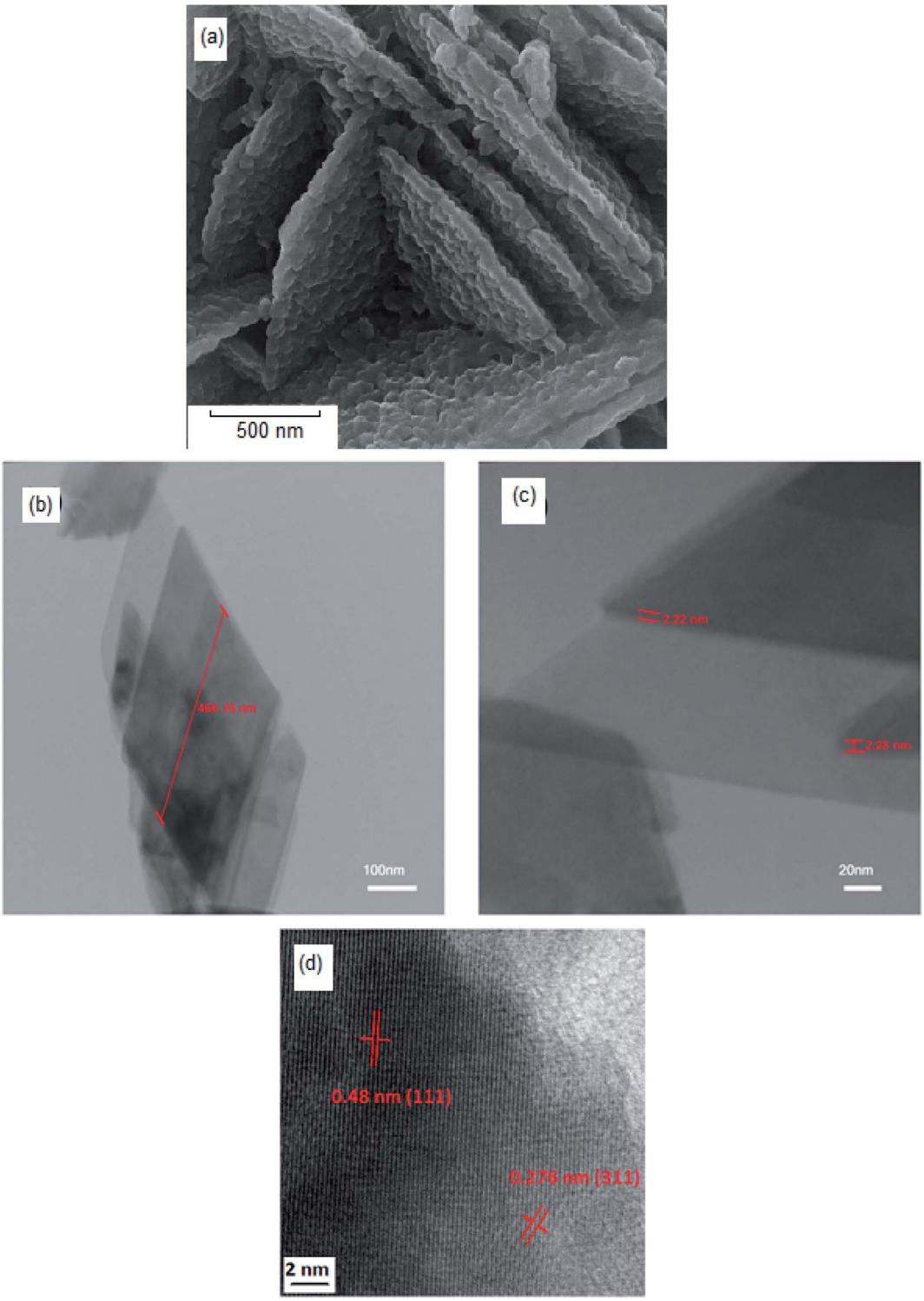

Fig. 5 (a) SEM image of hormone treated $NiFe_2O_4$ (sample 4), (b and c) TEM images, and (d) high-resolution TEM (HRTEM) of hormone treated $NiFe_2O_4$ (sample 4).

the amount of exhaust gases. Table 6 reports the results of various research papers on different nanofluid additives used in diesel to improve NO_x emission. By comparison, $NiFe_2O_4$ nanosheets + isodiesel and heavy diesel fuels induced a higher reduced level of NO_x emission during the combustion process (Fig. 7a). The NO_x emission in full load was 470 ppm, while it was 610 ppm for pure isodiesel. This shows that ferrite nanosheets act as a heat sink and reduce the cylinder temperature.[45]

Fig. 7b shows the curve of HC emission with brake power. Hydrocarbon emission is the result of incomplete combustion

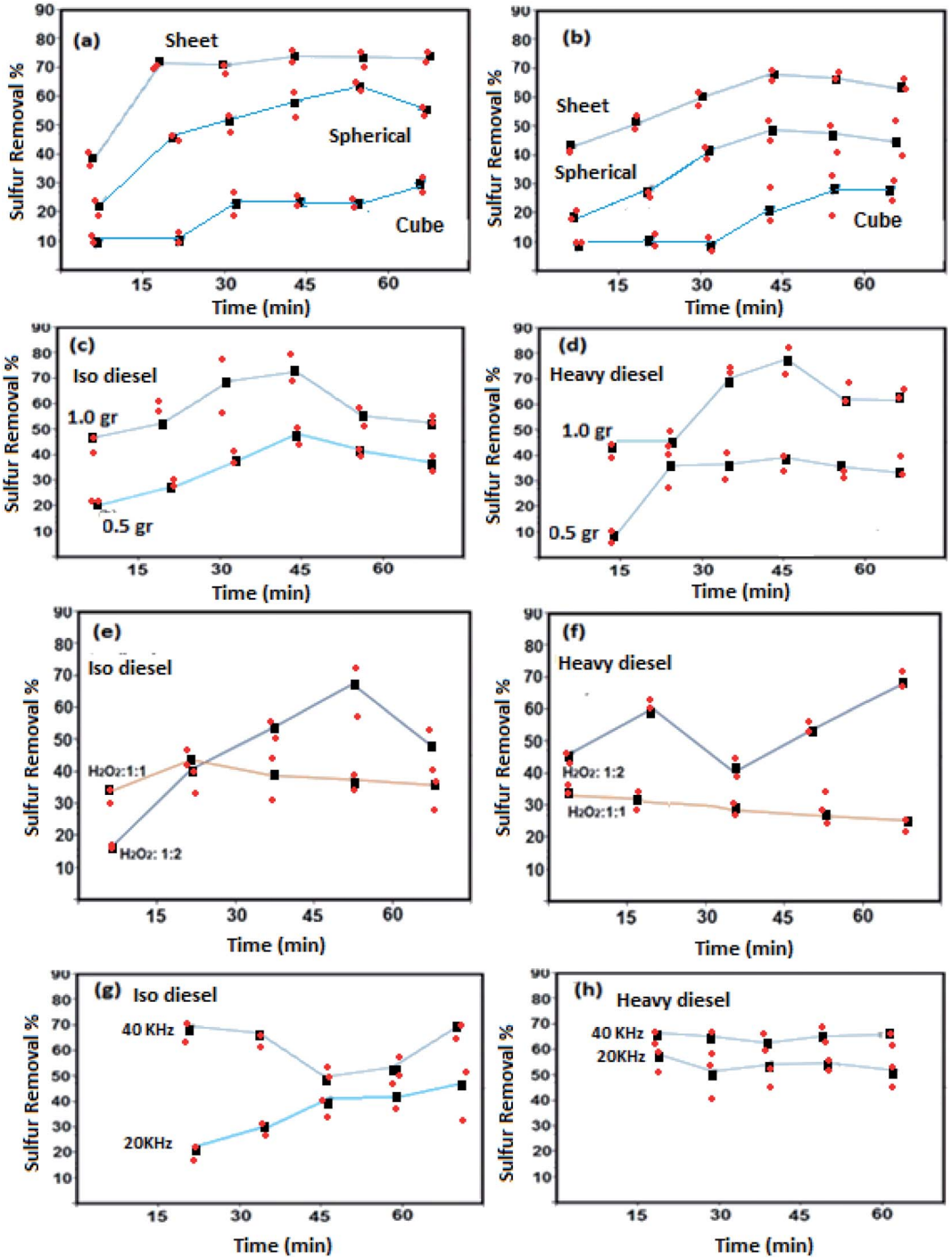

Fig. 6 Sulfur removal *via* variation in catalyst (sample 3, sample 4 and sample 5) morphologies: (a) iso diesel and (b) heavy diesel, and sulfur removal *via* variation in absorbent (hormone treated $NiFe_2O_4$) doses: (c) iso diesel and (d) heavy diesel. Sulfur removal *via* variation in H_2O_2 doses in the presence of hormone treated $NiFe_2O_4$ as the catalyst: (e) iso diesel and (f) heavy diesel. Sulfur removal *via* variation in frequency in the presence of hormone treated $NiFe_2O_4$ as a catalyst: (g) iso diesel and (h) heavy diesel.

of fuel. Most researchers reported that hydrocarbon emission is reduced by the addition of nano fuel additives because of higher evaporation rate and catalytic oxidation. Mehta RN[46] studied the effect of nano aluminum as an additive. A decrease of hydrocarbon emission up to 4% was observed for this additive doped water-diesel fuel. The activity of $NiFe_2O_4$ nanosheets is comparable with that of others reported on the combustion process. Complete combustion and sufficient oxygen availability can be further improved with $NiFe_2O_4$ nanosheets compared to no additive. In the case of isodiesel, $NiFe_2O_4$ in 1% concentration showed a 27 ppm HC emission level, compared with the 32 ppm HC emission level of no additives.[47]

Table 6 Engine performance by adding a nano additive in the diesel engine

Nano additive	Composition	NO_x emission %	Reference
Al	4%	>28	40
CNT	100 ppm	>30	41
Fe_3O_4	0.4%	>10	42
CeO_2	2%	>7	43
Platinum/cerium	2%	>20	44

CO emissions for different brake powers are illustrated in Fig. 7c. Lower CO emission was obtained with the Ni based additive because the diesel fuels with metal-based additives were burned well in the cylinders than diesel fuel without metal-based additives. The CO concentrations at different brake powers with 1% nanosheets were decreased by 5% in comparison to isodiesel fuel without additives. $NiFe_2O_4$ nanosheets behave as an oxidation catalyst, leading to reduced ignition delay.[48]

From Fig. 7d, it can be concluded that the $NiFe_2O_4$ nanosheet with a dose level of 1% has been emphasized for its affirmative effect when mixed with isodiesel, resulting in a 10% reduction of smoke emission. The main reason for this result is the presence of the $NiFe_2O_4$ nano additive in the isodiesel and heavy diesel, which improves ignition characteristics.

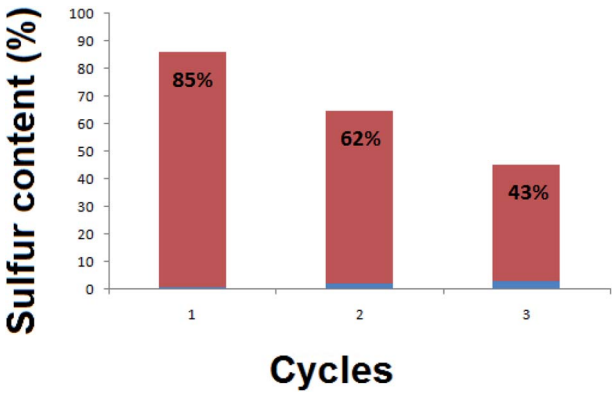

Fig. 8 Recycling of the hormone treated $NiFe_2O_4$ (sample 4) after generation.

Table 5 summarizes the properties of the feedstocks. The flash point is the lowest temperature that will produce sufficient vapor to provide a flammable mixture in the air. According to Table 5, an increase of 8 °C was observed in flash point after adding nanosheets at concentrations of 1% to isodiesel. By adding nano $NiFe_2O_4$, attraction forces between the particles increase and the flow from the liquid to gas phase reduces. The

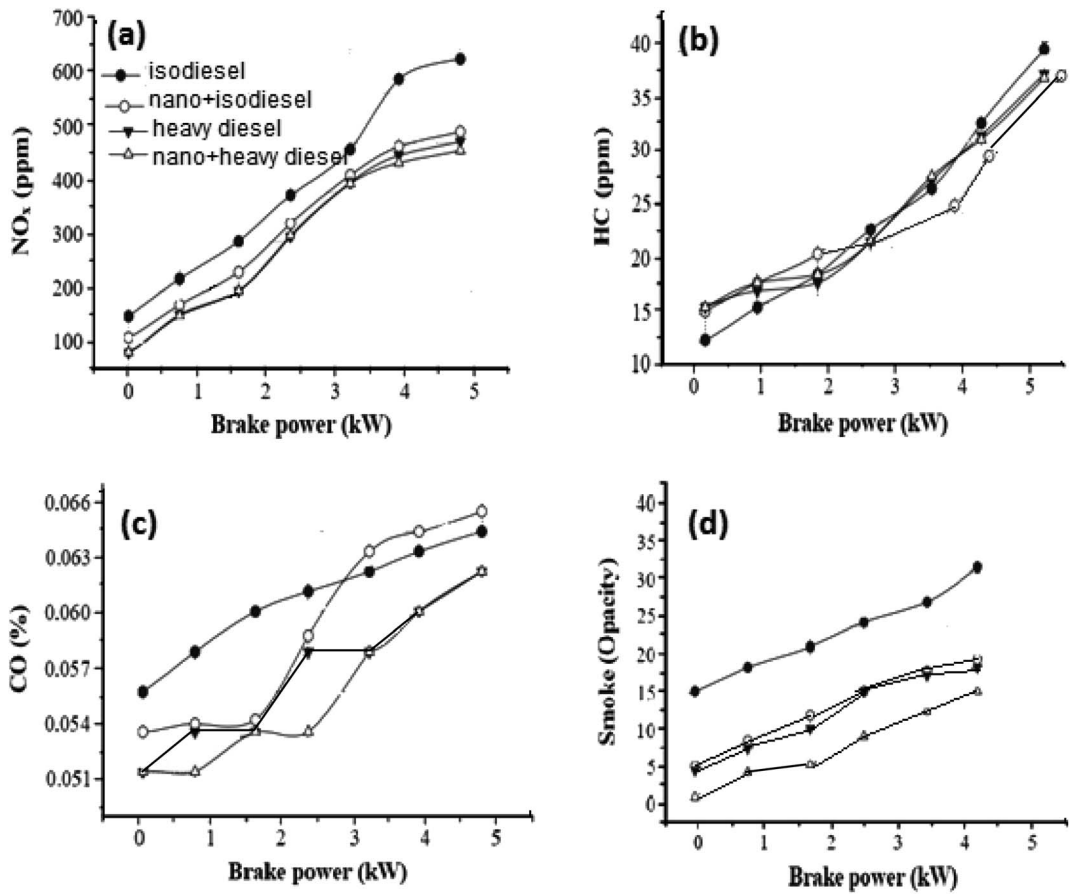

Fig. 7 Gas emission in the presence of hormone treated $NiFe_2O_4$ (1%) for iso diesel and heavy diesel: (a) NO_x, (b) HC, (c) CO and (d) smoke.

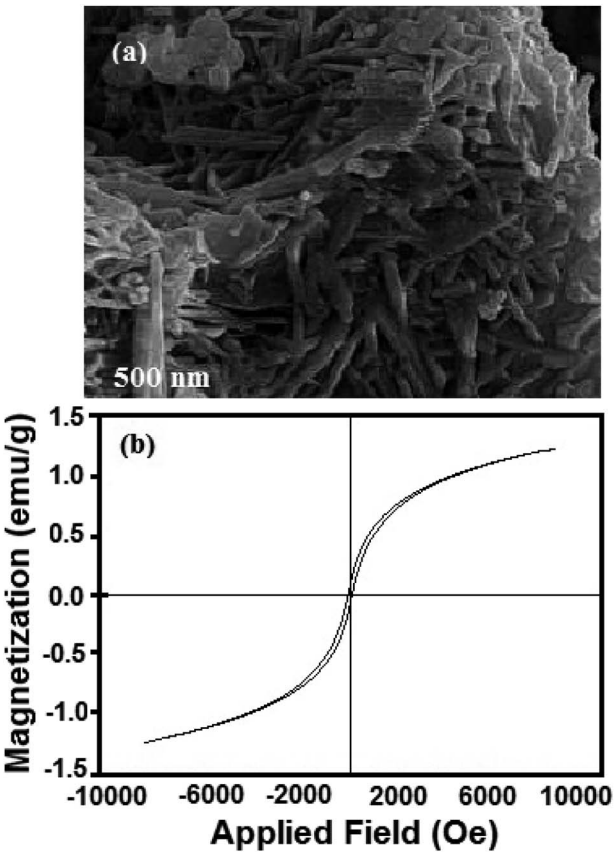

Fig. 9 (a) FESEM micrographs of regenerated $NiFe_2O_4$ nanosheets and (b) magnetization hysteresis loop of the regenerated sample.

kinematic viscosity is important to study the clean diesel production process. On average there is about a 10% change in viscosity for the two kinds of diesel (Table 5), which can be attributed to the catalytic nanoparticle addition in fuel. The resistance between layers of fluid increases by adding the nanocatalyst, which in turn affects the viscosity. High viscosities can generate deposits and increase emissions of greenhouse gases.[49]

3.4 Regeneration of the catalyst

Fig. 8 presents three cycles of regeneration of the catalyst ($NiFe_2O_4$ nanosheets). From the first cycle to the third one, the sulfur capacity decreased. Normally, $NiFe_2O_4$ does not maintain its adsorption capacity which becomes nearly zero after 4 cycles.

The regenerated $NiFe_2O_4$ was subjected to morphological and magnetic studies (Fig. 9). The FESEM micrograph (Fig. 9a) shows that the nanosheet morphology of the sample remains intact; however, it is less entangled as compared to the as-prepared sample (Fig. 3). The saturation magnetization (M_s), remanence magnetization (M_r) and coercivity (H_c) values for the sample are 1.0 emu g^{-1}, 0.05 emu g^{-1} and 78 Os, respectively. As compared to magnetization hysteresis of the as-prepared $NiFe_2O_4$ nanosheets (Fig. 4), the regenerated sample shows a 30% decrease in M_r, 22% in M_s, and 9% in H_c (Fig. 9b). The lower magnetization is due to the presence of an organic layer on the surface of $NiFe_2O_4$ nanosheets. The catalyst is attracted by an external magnetic field because of its ferromagnetic nature, which is important to form homogeneous systems.

4. Conclusions and future directions

$NiFe_2O_4$ nanostructures were synthesized by combined ultrasonic-combustion methods. Because of the unique chemical properties of $NiFe_2O_4$ nanosheets, T3 hormone (biotemplate) was used to control the shape and size. The physico–chemical properties of the hormone treated $NiFe_2O_4$ sample show that the as-prepared $NiFe_2O_4$ nanosheets have potential to be an efficient catalyst for the ODS process. Treatment of a real diesel led to 70% desulfurization under moderate conditions. Moreover, $NiFe_2O_4$ nanosheets are able to regenerate after quenching and this is one of the most critical factors to choose a right catalyst. To improve the engine performance an attempt is made and encouraging results were reported in detail. According to the analysis of our research paper, $NiFe_2O_4$ can be used as an additive in diesel due to its better combustion. Hence, the emission of noxious gases such as CO, HC, smoke and NO_x evidently decreases in isodiesel and heavy diesel. These advantages of $NiFe_2O_4$ nanosheets evidence their potential for environmental science and pollution research in the future. However, critical studies are in progress to trap the nanoparticles from the exhaust of the diesel engine.

Nomenclature

CO	Carbon monoxide (ppm)
HC	Hydrocarbons (ppm)
HRTEM	High resolution transmission electron microscopy
FESEM	Field emission scanning electron microscopy
VSM	Vibrating sample magnetometer
NO_x	Nitrogen oxides (ppm)
T3	3,5,3′-Triiodo-L-thyronine
TMB	Tetramethylbenzidine
bTDC	Before top dead centre

Conflicts of interest

The authors declare no competing interests.

Acknowledgements

The authors are grateful to the council of Iran National Science Foundation, INSF (97017837), contract (98002158) and University of Kashan for supporting this work by Grant No (159271/SM2).

References

1 P. Sivakumar, R. Ramesh, A. Ramanand, S. Ponnusamy and C. Muthamizhchelvan, Synthesis and characterization of

$NiFe_2O_4$ nanosheet via polymer assisted co-precipitation method, *Mater. Lett.*, 2011, **65**, 483–485.

2 R. Tholkappiyan and K. Vishista, Combustion synthesis of Mg–Er ferrite nanoparticles: Cation distribution and structural, optical, and magnetic properties, *Mater. Sci. Semicond. Process.*, 2015, **40**, 631–642.

3 Y. Qi, Y. Yang, X. Zhao, X. Liu, P. Wu and S. Xu, Controllable magnetic properties of cobalt ferrite particles derived from layered double hydroxide precursors, *Particuology*, 2010, **8**, 207–211.

4 M. Khandekar, R. Kambale, J. Patil, Y. Kolekar and S. Suryavanshi, Effect of calcination temperature on the structural and electrical properties of cobalt ferrite synthesized by combustion method, *J. Alloys Compd.*, 2011, **509**, 1861–1865.

5 P. Kumar, S. Sharma, M. Knobel and M. Singh, Effect of La3+ doping on the electric, dielectric and magnetic properties of cobalt ferrite processed by co-precipitation technique, *J. Alloys Compd.*, 2010, **508**, 115–118.

6 Y. Xu, G. Wu, H. Su, M. Shi, G. Yu and L. Wang, Magnetoelectric CoFe2O4/Pb(Zr0.53Ti0.47)O3 composite thin films of 2–2 type structure derived by a sol–gel process, *J. Alloys Compd.*, 2011, **509**, 3811–3816.

7 J. Peng, M. Hojamberdiev, Y. Xu, B. Cao, J. Wang and H. Wu, Hydrothermal synthesis and magnetic properties of gadolinium-doped CoFe2O4 nanoparticles, *J. Magn. Magn. Mater.*, 2011, **323**, 133–137.

8 X. Li, L. Wang, L. Xhang and S. Zhuo, A facile route to the synthesis of magnetically separable BiOBr/NiFe2O4 composites with enhanced photocatalytic performance, *Appl. Surf. Sci.*, 2017, **419**, 586–594.

9 N. Gupta, P. Jain, R. Rana and S. Shrivastava, Current Development in Synthesis and Characterization of Nickel Ferrite Nanoparticle, *Mater. Today Proc.*, 2017, **4**, 342–349.

10 T. Zhou, T. Zhang, Y. Zeng, R. Zhang, Z. LoU, J. Deng and L. Wang, Structure-driven efficient NiFe2O4 materials for ultra-fast response electronic sensing platform, *Sens. Actuators, B*, 2017, **255**, 1436–1444.

11 X. Liu, M. Liu and L. Zhang, Co-adsorption and sequential adsorption of the co-existence four heavy metal ions and three fluoroquinolones on the functionalized ferromagnetic 3D NiFe2O4 porous hollow microsphere, *J. Colloid Interface Sci.*, 2018, **511**, 135–144.

12 K. Senapati, C. Borgohain and P. Phukan, Synthesis of highly stable CoFe2O4 nanoparticles and their use as magnetically separable catalyst for Knoevenagel reaction in aqueous medium, *J. Mol. Catal. A Chem.*, 2011, **339**, 24–31.

13 C. Amutha, S. Thanikaikarasan, V. Ramadas, S. Asath Bahadur, B. Natarajan and R. Kalyani, Synthesis, characterization and antibacterial efficiency of ZnO nanoparticles using rice as soft bio-template, *Opt. – Int. J. Light Electron Opt.*, 2016, **127**, 4281–4286.

14 N. Hosni and K. Zehani, Synthesis of (2D) MNPs nanosheets of nickel ferrite using a low-cost co-precipitation process, *J. Mater. Sci. Eng.*, 2018, **232–235**, 48–54.

15 J. R. Katzer, M. P. Ramage and A. V Sapre, Petroleum refining: Poised for profound changes, *Chem. Eng. Prog.*, 2000, **96**, 41–51.

16 C. Song and X. Ma, New design approaches to ultra-clean diesel fuels by deep desulfurization and deep dearomatization, *Appl. Catal., B*, 2003, **41**, 207–238.

17 v. Lam, G. Li, C. Song, J. Chen, C. Fairbridge and R. Hui, A review of electrochemical desulfurization technologies for fossil fuels, *Fuel Process. Technol.*, 2012, **98**, 30–38.

18 X. Ma, L. Sun and C. Song, A new approach to deep desulfurization of gasoline, diesel fuel and jet fuel by selective adsorption for ultra-clean fuels and for fuel cell applications, *Catal. Today*, 2002, **77**, 107–116.

19 K. Kim and Y. Lee, Active phase of dispersed MoS_2 catalysts for slurry phase hydrocracking of vacuum residue, *J. Catal.*, 2019, **369**, 111–121.

20 M. Capel-Sanchez, J. Campos-Martin and J. Fierro, Removal of refractory organosulfur compounds via oxidation with hydrogen peroxide on amorphous Ti/SiO2 catalysts, *Energy Environ. Sci.*, 2010, **3**, 328–333.

21 C. Ma, D. Chen, F. Liu, X. Sun, F. Xiao and B. Dai, Oxidative desulfurization of a model fuel using ozone oxidation generated by dielectric barrier discharge plasma combined with Co_3O_4/γ-Al_2O_3 catalysis, *RSC Adv.*, 2015, **5**, 96945–96952.

22 K. Stanger and R. Angelici, Oxidation of benzothiophenes using tert-amyl hydroperoxide, *Energy. Fuel.*, 2006, **20**, 1757–1760.

23 M. Capel-Sanchez, P. Perez-Presas, J. Campos-Martin and J. Fierro, Highly efficient deep desulfurization of fuels by chemical oxidation, *Catal. Today*, 2010, **157**, 390–396.

24 H. Yokomura, S. Kohketsu and K. Mori, EGR System in a Turbocharged and Intercooled Heavy-Duty Diesel Engine: Expansion of EGR Area with Venturi EGR System, *Mitsubishi. Tech. Review.*, 2003, **15**, http://www.mitsubishimotors.com.

25 S. Vellaiyan and K. Amirthagadadeswaran, The role of water-in-diesel emulsion and its additives on diesel engine performance and emission levels: A retrospective review, *Alex. Eng.*, 2016, **3**, 2463–2472.

26 K. Vijaya and P. shailesh, Performance and emission analysis of diesel engine with design modifications on piston crown, *Intern. Amb. Energy*, 2020, **41**(12), 1336–1341.

27 V. Sajith, C. B. Sobhan and G. P. Peterson, Experimental Investigation on the Effects of Cerium Oxide Nano Particle Fuel Additives on Biodiesel, *Adv. Mech. Eng.*, 2010, 581407.

28 S. Nakkeeran and J. H. Hussain, Innovative technique for running a petrol engine with diesel as a fuel, International, *J. Pure. Appl. Math.*, 2017, **116**, 41–44.

29 D. C. Mcculloch, Catalytic Hydrotreating in Petroleum Refining, *Appl. Ind. Catal.*, 1983, 69–121.

30 C. Bartholomew, Catalyst Deactivation in Hydrotreating of Residue, *Catal. Hydroprocessing Pet. Distill.*, 2010, 1–32.

31 J. Speight, *The desulfurization of Heavy Oils Residua*, Marcel Dekker, 2nd edn, 1981.

32 C. L. Garcia and J. A. Lercher, Adsorption of hydrogen sulfide on ZSM 5 zeolites, *J. Phys. Chem.*, 1992, **96**, 2230–2235.

33 A. J. Hernández-Maldonado, G. Qi and R. T. Yang, Desulfurization of commercial fuels by π-complexation: Monolayer CuCl/γ-Al2O3, *Appl. Catal., B*, 2005, **61**, 212–218.
34 *Principle of the Procedure; Free T3 (Triiodothyronine) MICRO-ELISA Test Kit*, n.d, https://www.leinco.com/ELISA-Kit/Triiodothyronine/pdf/T183.pdf, accessed October 17, 2017.
35 S. Das and V. Jayaraman, A comprehensive review on structures and gas sensors, *Prog. Mater. Sci.*, 2014, **66**, 112–255.
36 A. Pradeep and G. Chandrasekaran, FTIR study of Ni, Cu and Zn substituted nano-particles of MgFe2O4, *Mater. Lett.*, 2006, **60**, 371–374.
37 N. Rezlecu, E. Rezlescu, P. D. Popa, C. Doroftwi and M. Ignat, Comparative study between catalysts properties of simple spinel ferrites powders prepared by self-combustion route, *Rom. Rep. Phys.*, 2013, **65**, 1348–1356.
38 L. Zhiming, G. Xiaolin, T. Fei and Z. Renxian, New insights into the effect of morphology on catalytic properties of MnOx–CeO_2 mixed oxides for chlorobenzene degradation, *RSC Adv.*, 2018, **45**, 25283–25291.
39 C. Petrier, B. David and S. Laguian, Chemosphere Ultrasonic degradation at 20 kHz and 500 kHz of atrazine and pentachlorophenol in aqueous solution: Preliminary results, *chemosphere*, 1996, **32**, 1709–1718.
40 R. N. Mehta, M. Chakraborty and P. A. Parikh, Impact of hydrogen generated by splitting water with nanosilicon and nano-aluminum on diesel engine performance, *Int. J. Hydrogen Energy*, 2014, **39**, 8098–8105.
41 N. Singh and R. S. Bharj, Effect of CNT-emulsified fuel on performance, emission and combustion characteristics of four stroke diesel engine, *Int J Current Eng Tech*, 2015, **5**(1), 477–485.
42 A. S. Farzad, E. E. Bajestan and M. Mir, Effects of magnetic nanofluid fuel combustion on the performance and emission characteristics, *J. Dispers. Sci. Technol.*, 2014, **35**, 1745–1750.
43 V. Sajith, C. B. Sobhan and G. P. Peterson, Experimental investigations on the effects of cerium oxide nanoparticles fuel additives on biodiesel, *Adv Mech Eng*, 2010, 1–6.
44 A. Keskin, M. Guru and D. Altiparmak, Influence of metallic based fuel additives on performance and exhaust emissions of diesel engine, *Energy Convers Manag*, 2011, **52**, 60–65.
45 F. Ansari, A. Sobhani and M. Salavati-Niasari, Simple sol-gel synthesis and characterization of new CoTiO3/CoFe2O4 nanocomposite by using liquid glucose, maltose and starch as fuel, capping and reducing agents, *Journal of colloid and interface science*, 2018, **514**, 723–732.
46 R. N. Mehta, M. Chakraborty and P. A. Parikh, Impact of hydrogen generated by splitting water with nanosilicon and nano-aluminum on diesel engine performance, *Int. J. Hydrogen Energy*, 2014, **39**, 8098–8105.
47 M. Mirzajanzadeh, *et al.*, Novel Soluble Nano-Catalyst in Diesel-Biodiesel Fuel Blends to Improve Diesel Ngines Performance and Reduce Exhaust, *Emissions Fuel*, 2015, **139**, 374–382.
48 M. Guru, U. Karakaya, D. Altiparmak and A. Alicilar, Improvement of diesel fuel properties by using additives, *Energy. Convers. Manag.*, 2002, **43**, 1021–1025.
49 I. Nwadike, *et al.*, Cold Flow properties and kinematic viscosity of biodiesel, *Uni. Chem*, 2013, **1**(4), 135–141.